Hydroxyapatite nanoparticles-cell interaction: New approaches to disclose the fate of membrane-bound and internalised nanoparticles

Mar Bonany [a,b,c], Ana Joaquina Pérez-Berná [d], Tanja Dučić [d], Eva Pereiro [d],
Helena Martin-Gómez [a,b], Carlos Mas-Moruno [a,b,c], Sabine van Rijt [e], Zhitong Zhao [a,g],
Montserrat Espanol [a,b,c,*], Maria-Pau Ginebra [a,b,c,f]

[a] Biomaterials, Biomechanics and Tissue Engineering Group, Department of Materials Science and Engineering, Universitat Politècnica de Catalunya (UPC), 08019 Barcelona, Spain
[b] Barcelona Research Centre in Multiscale Science and Engineering, UPC, 08019 Barcelona, Spain
[c] Biomedical Engineering Research Center (CREB), UPC, 08028 Barcelona, Spain
[d] MISTRAL Beamline Experiments Division, ALBA Synchrotron Light Source, 08290 Barcelona, Spain
[e] Department of Instructive Biomaterials Engineering, MERLN Institute for Technology-Inspired Regenerative Medicine, Maastricht University, 6200, MD, Maastricht, the Netherlands
[f] Institute for Bioengineering of Catalonia (IBEC), Barcelona Institute of Science and Technology, 08028 Barcelona, Spain
[g] School of Materials Science and Engineering, Nanyang Technological University, Singapore 639798, Singapore

ARTICLE INFO

ABSTRACT

Hydroxyapatite nanoparticles are popular tools in bone regeneration, but they have also been used for gene delivery and as anticancer drugs. Understanding their mechanism of action, particularly for the latter application, is crucial to predict their toxicity. To this end, we aimed to elucidate the importance of nanoparticle membrane interactions in the cytotoxicity of MG-63 cells using two different types of nanoparticles. In addition, conventional techniques for studying nanoparticle internalisation were evaluated and compared with newer and less exploited approaches. Hydroxyapatite and magnesium-doped hydroxyapatite nanoparticles were used as suspensions or compacted as specular discs. Comparison between cells seeded on the discs and those supplemented with the nanoparticles allowed direct interaction of the cell membrane with the material to be ruled out as the main mechanism of toxicity. In addition, standard techniques such as flow cytometry were inconclusive when used to assess nanoparticles toxicity. Interestingly, the use of intracellular calcium fluorescent probes revealed the presence of a high number of calcium-rich vesicles after nanoparticle supplementation in cell culture. These structures could not be detected by transmission electron microscopy due to their liquid content. However, by using cryo-soft X-ray imaging, which was used to visualise the cellular ultrastructure without further treatment other than vitrification and to quantify the linear absorption coefficient of each organelle, it was possible to identify them as multivesicular bodies, potentially acting as calcium stores. In the study, an advanced state of degradation of the hydroxyapatite and magnesium-doped hydroxyapatite nanoparticles within MG-63 cells was observed. Overall, we demonstrate that the combination of fluorescent calcium probes together with cryo-SXT is an excellent approach to investigate intracellular calcium, especially when found in its soluble form.

1. Introduction

Over the past few years, the application of hydroxyapatite (HA) in the form of nanoparticles (NPs) has received considerable attention as a transfection vehicle for the transport of genetic material into cells and in bone regeneration [1–4]. HA NPs have also been proposed as a useful tool in cancer therapy. It has been observed that they were able to cause cell death of several cancer cell types whilst having minimal side effects on healthy cells [5–9]. Moreover, ion-doped HA NPs have been investigated for cancer treatment showing improved cytotoxic potential

towards cancer cells and being more selective than non-doped HA [10]. Actually, ions are particularly interesting in cancer treatment, as it has been demonstrated that some specific cancer cells have ionic channel dysregulations in their membrane, *e.g.* TRPM7 magnesium transporter is upregulated in breast and pancreatic cancer, as well as in osteosarcoma MG-63 cell line [11–15]. However, the exact mechanisms of cell death are still under debate.

Three different scenarios which can potentially drive towards cytotoxicity can be anticipated: (1) reactivity of the NPs with the surrounding fluids, causing the release or depletion of ions and proteins crucial for cells; (2) NP interaction with cell membrane receptors that may induce apoptotic signalling cascades; and (3) NPs internalisation and subsequent effects inside the cell. Furthermore, these scenarios will be affected by the aggregation state of the NPs. Indeed, the hydrodynamic properties of aggregated nanomaterials (including diffusion and sedimentation, as well as their interaction with the cell membrane and internalisation), may change with respect to individual nanoparticles [16].

The most accepted hypothesis to explain cytotoxicity is based on the third assumption and relies on the degradability of the NPs upon internalisation. Indeed, after HA NPs uptake by endocytosis, they degrade under the acidic conditions in the lysosome, yielding an increase of calcium and phosphorus ions. Whereas a slow and sustained dissolution of HA in the lysosomes would be innocuous to cells and would benefit transfection [17], a more efficient and fast internalisation of NPs would release a high concentration of calcium ions that would lead to cell death [18]. This has been hypothesised to be caused either by apoptosis, *i.e.* programmed cell death, triggered by a disruption of cell homeostasis [19] or by necrosis, when the rapid dissolution of calcium phosphate NPs in the lysosomes causes an imbalance of the osmotic pressure that results in their rupture [20,21].

In order to describe in detail the HA NPs mode of action, it is necessary to have reliable methods to assess not only their internalisation but also their dissolution once inside the cells. Internalised NPs can be detected either by transmission electron microscopy or by tracking fluorescently labelled NPs with different techniques (*e.g.* flow cytometry, fluorescent microscopy, *etc.*). However, with some of these techniques it is not always possible to differentiate the cell surface-associated particles from the ones internalised into the cells [22,23]. Moreover, since these strategies rely on the visualisation of pristine NPs, they are insufficient to predict their toxicity, which requires HA NPs solubilisation. Therefore, correlating the amount of internalised NPs and their cytotoxic effect can be challenging [24]. Thereby, various studies have used calcium probes to measure intracellular calcium levels and thus, to check HA NPs intracellular dissolution [18,20,21,24]. In this sense, Neumann et al. determined calcium uptake by T24 cells during the standard calcium phosphate transfection method using isotope labelling with 45 Ca [18]; Liu et al. instead used the Fluo-3 AM probe in HepG2 cells treated with HA NPs to quantify intracellular calcium by analysing the fluorescent intensity caused by intracellular Ca^{2+} binding to Fluo-3 [20]. Similarly, Huang et al. used Fluo-4 AM for quantification of intracellular calcium in A7r5 cells treated with HA NPs of different shapes [21]. Despite the relatively spread used of Ca probes as chemical fluorescent ion indicators, their most important problem is compartmentalisation, which means that the indicator can be selectively trapped in some intracellular organelles, making its distribution heterogeneous throughout the cell [25].

In addition to the above methods, in this study we propose the use of cryo-soft X-ray tomography as a novel approach to analyse the ultrastructure of intact and unstained cells, as well as to obtain quantitative data on the linear absorption coefficient of each organelle, which relates to its composition. Moreover, various authors have used this technique to obtain X-ray images at the Ca edge energy to help unambiguously identify calcium deposits in cells in their native state [26–28]. Compared to calcium imaging, this technique offers the advantage of visualising soluble calcium-rich vesicles without losing the information of solid

calcium material.

Beyond the effects associated with NP internalisation, little attention has been paid in the literature to the influence of ionic exchanges between HA NPs and the surrounding fluids on cell viability [10,29,30]. This may be relevant, as drastic ionic fluctuations, especially of calcium, phosphorus and magnesium, elicited by nanostructured hydroxyapatite materials, have been reported to result in cytotoxicity [31–33]. On the other hand, to the best of our knowledge, there is no literature discerning between the contribution of cell membrane-bound HA and internalised HA to cell viability.

In this context, the objectives of the present work are: (1) to unravel the influence of nanoparticle-cell membrane interaction on cell cytotoxicity, leading to a better understanding of the mechanisms behind the use of HA and magnesium-doped HA (MgHA) NPs in cancer treatment applications; and (2) to investigate fundamental aspects regarding the NPs internalisation and fate within the cells by comparing the use of conventional techniques such as flow cytometry, to calcium fluorescence probes and cryo-soft X-ray tomography to track calcium-rich vesicles and the degradation state of internalised HA NPs.

2. Experimental

2.1. Synthesis and characterisation of non-doped and magnesium-doped hydroxyapatite nanoparticles

Non-doped and magnesium-doped hydroxyapatite nanoparticles (HA NPs and MgHA NPs, respectively) were obtained by the neutralisation of calcium hydroxide with ortho-phosphoric acid, as described elsewhere [10]. Briefly, 100 ml 200 mM H_3PO_4 (85 wt% pure, Panreac) was added dropwise into a 100 ml solution of 333 mM $Ca(OH)_2$ (96 wt% pure, Fluka) at a rate of 1 ml min^{-1}. The reaction, described in Eq. (1), was performed under constant stirring at 40 °C in thermojacketed vessels and the pH was continuously monitored.

$$10Ca(OH)_2 + 6H_3PO_4 \rightarrow Ca_{10}(PO_4)_6(OH)_2 + 18H_2O \qquad (1)$$
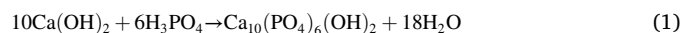
At pH 8, the reaction was stopped and the solution was stirred for 30 min at 40 °C. Afterwards, it was left to mature overnight at room temperature. The suspension was then rinsed three times with bi-distilled water, performing centrifugation cycles of 5 min at 800*g* (5430 R, Eppendorf). Finally, the product was freeze-dried (Cryodos, Telstar).

The synthesis of MgHA NPs was done similarly, with the incorporation of magnesium chloride powder (MgCl$_2$·6 H$_2$O, 99 wt% pure, PanReac) into the calcium hydroxide solution prior to H$_3$PO$_4$ addition. The final Mg^{2+} content in these NPs was ≈2.3 wt% [10].

The NPs were suspended in bi-distilled water to a final concentration of 10 mg ml^{-1} and sonicated with a high-frequency ultrasound probe sonicator (450D, Branson Digital) to improve their deagglomeration. A 3 mm diameter tip was used with 40 % amplitude for 2 min in an ice bath. In addition, specular discs were prepared by compacting 200 mg of the freeze-dried NPs into 10-mm diameter moulds and applying a uniaxial pressure of 3 tons for 2 min.

Characterisation of the NPs comprised analysis of the phase composition by X-ray diffraction (XRD, D8 Advance, Bruker) using Cu Kα radiation at 40 kV and 40 mA. Data were collected with a step size of 0.02° over the 2θ range from 20 to 40° with a counting time of 2 s per step. Phase identification was accomplished by comparing the results with the standard patterns of HA (ICDD PDF 09-0432). In addition, morphological evaluation of the NPs was assessed by transmission electron microscopy (TEM, JEM-1010, JEOL) after soaking a 300-mesh carbon-coated copper grid into the NPs suspensions. Finally, the surface morphology of the discs was studied by scanning electron microscopy (SEM, JSM-7001F, JEOL). Prior to the observation, the samples were coated with a thin gold-palladium layer using vapour deposition (SCD 004, Balzers).

2.2. Fluorescent functionalisation of the nanoparticles

In order to track the NPs, a fluorescent biomolecule was attached to HA by means of strong hydrogen bonds *via* catechol groups [34]. To this end, a custom-made linear peptide containing DOPA and carboxyfluorescein (CF) (Table 1) was synthesised by solid-phase peptide synthesis (SPPS) following the Fmoc/tBu strategy and using Rink Amide MBHA resin (243 mg, 0.45 mmol g^{-1}) as solid support, according to the protocols optimised in our group [35]. The peptide was used with a purity of $\geq$90 %, as determined by reversed-phase analytical high-performance liquid chromatography (RP-HPLC, Prominence UFLC XR, Shimadzu).

The lyophilised peptide was dissolved in distilled water to a series of concentration from 500 μM down to 1 μM, adjusting the pH to 7. CF alone was also studied at the same concentrations and pH. The functionalisation of the HA NPs was accomplished by mixing under constant stirring 200 μl of 1 wt% NPs suspension and 100 μl of either peptide or CF solutions for 2 h. The resulting suspension was centrifuged and rinsed three times with bi-distilled water and re-suspended to a final concentration of 1 wt%. After functionalisation, supernatants and washing residues were collected and their fluorescent intensity was measured by means of a microplate reader (Synergy HTX, BioTek Instruments). Knowing the difference between the initial amount of peptide added and the quantity that remained in the supernatants, data were correlated to a calibration curve to determine the final concentration of peptide adsorbed on the NPs.

The fluorescent NPs (*i.e.* HA-F and MgHA-F) functionalised using a concentration of 500 μM of the fluorescent peptide were selected for the cell culture studies. In addition, direct fluorescence intensity was measured in 100 μg ml^{-1} NP suspension by means of a fluorescence spectrophotometer (Cary Eclipse, Agilent). Finally, the zeta potential of the different NPs (*i.e.* HA and MgHA, before and after functionalisation) was measured in 300 μg ml^{-1} NPs suspensions using a Zetasizer Nano (Malvern Panalytical).

2.3. Cell culture

Human osteosarcoma MG-63 cells (ATCC) were cultured in Dulbecco's Modified Eagle medium (DMEM) supplemented with 10 % foetal bovine serum (FBS), 20 mM 4-(2-hydroxyethyl)-1-piperazineethanesulfonic acid buffer (HEPES), 2 mM L-glutamine, 50 U ml^{-1} penicillin and 50 μg ml^{-1} streptomycin (all from Gibco), in a 95 % humidified atmosphere containing 5 % CO$_2$ at 37 °C. Confluent cells were detached using TrypLE Express (Gibco).

For the cell culture studies, the NPs suspensions were sonicated in a bath sonicator (JP Selecta) for 5 min before their addition to the cell culture media, in order to avoid agglomerates. The experiments were carried out in serum-containing (*i.e.* NPs supplemented or cells seeded on discs in 10 % FBS-containing media, FBS+) and in serum-free (FBS−) conditions to assess the influence of the protein corona. Moreover, different time points were studied, ranging from 3 to 24 h, depending on the study, and the supplemented dose of NPs was 100 μg ml^{-1} in all cases. Controls were prepared seeding the cells on sterile coverslips ($\varnothing$ = 10 mm).

2.4. Nanoparticles – cell membrane interaction

MG-63 cells were seeded on sterile coverslips ($\varnothing$ = 10 mm) in a 48-well plate at a density of 25,000 cells per well and incubated overnight to allow cell adhesion. The following day, culture media containing 100 μg ml^{-1} of each NPs were prepared and supplemented to the cells. At the same time, previously compacted discs were sterilised with ethanol 70 % for 30 min and rinsed with phosphate-buffered saline (PBS, Gibco). Afterwards, cells were seeded on top of them and left 4 h for interaction. The morphology of the cells was assessed by confocal microscopy (LSM 800, Zeiss) using acridine orange staining (AO, Sigma-Aldrich). Cell morphology was further analysed by scanning electron microscopy (SEM, JSM-7001F, JEOL). To do so, samples were fixed with 2.5 % glutaraldehyde (Sigma-Aldrich) in PBS for 1 h at 4 °C. Subsequently, fixed samples were rinsed with PBS and dehydrated in an increasing series of ethanol solutions. Dried discs and coverslips were covered with a thin gold-palladium layer using vapour deposition (SCD 004, Balzers). To quantify the results, a cytotoxicity assay was carried out using WST-1 reagent (Roche) and following the manufacturer's indications.

2.5. Flow cytometry assay

For the flow cytometry (FC) studies, MG-63 cells were seeded on 6-well plates at a density of 300,000 cells per well and incubated overnight. The following day, fresh culture media containing 100 μg ml^{-1} of functionalised NPs (*i.e.* HA-F and MgHA-F) were supplemented into the samples. After 4, 6 and 24 h of exposure, cells were detached from the wells using trypsin and the supernatant was removed after centrifugation. The pellet was rinsed and re-dispersed in PBS prior to analysis by flow cytometry (Accuri C6, BD Biosciences) at an emission wavelength of 488 nm. Controls were used to gate living cells and to determine the fluorescence threshold. A total of 10,000 events were evaluated for each condition, except for serum-free samples at 24 h, due to cell death. Data analysis was performed with FlowJo software (FlowJo LLC, version 10). In addition, cells supplemented with functionalised NPs were imaged in a confocal fluorescence microscope (LSM 800, Zeiss) to assess aggregation of NPs during cell culture. Before visualisation, cells were fixed and stained with Alexa Fluor 568-phalloidin (Thermo Fisher) and 4′,6-diamidino-2-phenylindole (DAPI, Sigma-Aldrich) after 4 h of interaction with the materials.

2.6. Intracellular calcium evaluation

For the quantification of intracellular calcium, MG-63 cells were seeded on a black 96-well plate at a density of 10,000 cells per well and incubated overnight, whereas for the imaging 25,000 cells were seeded on sterile coverslips in a 48-well plate. The following day, culture media containing either HA or MgHA NPs were supplemented to the cells. An apoptosis control was also tested by adding H$_2$O$_2$ in the medium at a final concentration of 200 μM, instead of NPs. After 3 h of incubation, cells were stained with Fluo-4 AM intracellular calcium indicator (Thermo Fisher) following the manufacturer's indications. The green intensity was quantified in a fluorescence microplate reader (Synergy HTX, BioTek Instruments) and the imaging was performed in a confocal microscope (LSM 800, Zeiss).

2.7. Transmission electron microscopy

For TEM imaging, 90-mm Petri dishes were coated with poly-L-lysine prior to MG-63 seeding. After overnight cell attachment, FBS-free culture media containing each type of NPs were supplemented to the cells. A control sample without NPs was also studied. The cells were exposed for 3 h and afterwards fixed with 2.5 % glutaraldehyde (Sigma-Aldrich) in 0.1 M phosphate buffer (PB) for 1 h and detached with the help of a

Table 1
Chemical sequence of the fluorescent peptide and properties.

Sequence[a]	Purity (%)[b]	t_R (min)[b]	Molecular weight (g mol^{-1})
CF-(Ahx)$_2$-βAla-DOPA$_2$-NH$_2$	90.3	6.127	1031.07

[a] CF: (5)6-carboxyfluorescein; Ahx: 6-aminohexanoic acid; βAla: beta-alanine; DOPA: L-3,4-dihydroxyphenylalanine.
[b] Characterised by HPLC using a reversed-phase XBridge (Waters) C18 column (4.6 mm × 100 mm, 3.5 μm) and a linear gradient from 20:100 (0.036 % TFA in ACN/0.045 % TFA in H$_2$O) in 8 min at 25 °C.

scrapper to form a pellet. The pellet was rinsed and put in contact with a solution of 1 wt% OsO$_4$ and 0.8 wt% potassium ferricyanide for 2 h. Subsequently, it was dehydrated in an ascending series of acetone and infiltrated with EPON resin. Finally, blocks were sectioned with an ultramicrotome (Ultracut UCT, Leica) and the sections were stained with 2 wt% uranyl acetate and imaged with an optical microscope (DM2000 LED, Leica) and TEM (Tecnai Spirit Twin, FEI).

2.8. Cryo-soft X-ray tomography

For cryo-soft X-ray tomography (cryo-SXT), gold Quantifoil R2/2 G200F1 finder grids were coated with fibronectin (Sigma). Cells were seeded on the grids and incubated overnight. The following day, culture media without FBS containing NPs was supplemented to the cells. After 3 h of incubation, the grids were rinsed with PBS and immediately frozen in liquid ethane cooled with liquid nitrogen using an automatic plunge freezer for the bare grid technique (EM GP, Leica Microsystems). The samples were initially examined by means of a cryo-visible light microscope (Axioscope, Zeiss) provided with a cryo-stage (CMS196, Linkam Scientific). Samples were stored under liquid nitrogen and subsequently kept under cryogenic conditions at all times during the measurements by X-ray microscopy in the vitrified state. Cryo-SXT imaging was performed at the MISTRAL beamline of the ALBA Synchrotron light source. Tomographic data was collected at 520 eV, irradiating the samples for 2–10 s per projection. 520 eV is the energy range in which water is transparent for X-rays and there are mostly absorbed by carbon, allowing the visualisation of biological material. In tomographic setup, images obtained at different sample orientations are computationally combined to produce a three-dimensional (3D) image, permitting the 3D representation of the sub-cellular ultrastructure of whole intact cells. A tilt series was acquired for each cell using an angular step of 1° on a 70° angular range.

Each transmission projection image of the tilt series was normalised using flat-field. This process also considers the possibly different exposure time, as well as the slight decrease of the electron beam current during the acquisition. In order to increase the image quality, wiener deconvolution taking into account the experimental impulse response of the optical system [36] was applied to the normalised data. Finally, the Naperian logarithm was used to reconstruct the linear absorption coefficient (LAC). The resulting stacks were then loaded into IMOD software [37] and the individual projections were aligned to the common tilt-axis using the internal cellular structures as markers. Afterwards, the aligned stacks were reconstructed with algebraic reconstruction techniques (ART) [38]. The visualisation, segmentation and quantification of the volumes were carried out using Amira 3D software (Thermo Fisher). Each voxel of the reconstructed tomogram represents the LAC (μ_l, in cm^{-1}) of the material contained in it, as it is related to the measured transmission signal I through the Beer-Lambert law (Eq. (2)):

$$\text{Voxel} = \mu_l = -ln\left(\frac{I}{I_0}\right) = \int \mu_l(z)dz \qquad (2)$$

where μ corresponds to the mass absorption coefficient of the cell structure (cm^2 g^{-1}), I_0 to the incoming flux, and z to the thickness of the material.

2.9. Statistical analysis

Data distribution was checked with Shapiro-Wilk test. Significant differences between samples were determined using non-parametric Kruskal-Wallis test followed by multiple pairwise comparisons. Significance level was set for $p < 0.05$. Statistical analysis was performed using Minitab 19. All data are reported as mean of triplicate wells ± standard error of the mean (the experiments were duplicated or triplicated to confirm tendencies).

3. Results and discussion

3.1. Characterisation of the nanoparticles

Hydroxyapatite (HA) nanoparticles (NPs) were synthesised using a wet precipitation method, obtaining non-doped HA and magnesium-doped HA (MgHA) powders. Fig. 1A shows the XRD results of the synthesised NPs. All peaks matched those corresponding to HA (ICDD PDF 09-0432) with no secondary crystalline phases detected, demonstrating the precipitation of phase pure apatite (likely a calcium-deficient apatite considering the presence of B-type carbonation, as proved in our previous work [7]). For simplicity, we will refer to the synthesised apatite as hydroxyapatite (HA). Moreover, the broad peaks indicated the poor crystallinity of the powders obtained. As expected, magnesium doping caused a slight shift of the (002) diffraction peak, which correlates with the lattice contraction caused by the incorporation of Mg into the HA structure substituting Ca ions, due to the smaller ionic radius of the Mg cation compared to Ca [39].

No differences in the morphology of the two types of NPs were observed (Fig. 1B), both consisting of needle-like crystals with sizes of around 150 nm in length and 20 nm in width. The discs obtained by NPs compaction showed a homogeneous surface microstructure, with specular faces (Fig. 1C). A close-up view in the insets allowed to observed the individual nanoparticles in the discs by SEM. Immersion of the discs in culture medium did not alter their surface and no particles were dislodged from the samples, indicating excellent compaction.

3.2. Functionalisation of the nanoparticles

L-3,4-Dihydroxyphenylalanine (DOPA) is a molecule that presents an excellent affinity for hydroxyapatite through the catechol groups [34,40]. Although the adsorption of DOPA to HA NPs has been explored to enhance the osteoconductive properties of scaffolds and to improve protein adhesion for drug delivery purposes [41,42], to the best of our knowledge this is the first time that it is used to fluorescently label HA NPs, by combining it with a fluorescent molecule such as carboxyfluorescein (CF).

The evaluation of the adsorption capacity of either CF or the DOPA-CF peptide on the nanoparticles was done by measuring the difference in the concentration of the staining solution before and after NPs incubation. The direct adsorption of CF on the NPs was almost non-existent, or binding was so weak that the fluorophore was lost during the subsequent rinsing steps (data not reported). Fig. 2A illustrates the quantity of DOPA-CF peptide adsorbed on the surface of the NPs, for both non-doped (HA-F) and magnesium-doped (MgHA-F) after rinsing. It is observed that in the case of non-doped NPs, the adsorption of DOPA-CF was about half of the concentration added, whereas in the case of MgHA powders, this adsorption was slightly lower, around 40 % of the initially added peptide. This reduction of adsorbed DOPA-CF was further confirmed by direct fluorescence intensity data, shown in Fig. 2B, where the intensity of MgHA-F NPs was 80 % with respect to the HA-F sample. This variation might be due to physicochemical differences between both types of nanoparticles. After functionalisation of the NPs, various rinsing steps with bi-distilled water were carried out to eliminate the non-adhered peptide and the fluorescence intensity of the supernatants was measured. It is worth to mention that the intensity in the first rinse after vortexing of the fluorescently labelled NPs was about 5 %, which explained the excellent binding between DOPA-CF and the NPs.

The zeta potential of the NPs measured in water is displayed in Fig. 2C, revealing a slightly negative surface charge for the pristine nanoparticles. When functionalising the NPs with the fluorescent peptide, the surface charge decreased to −13 mV for both HA-F and MgHA-F, which confirmed the success in the functionalisation of the NPs.
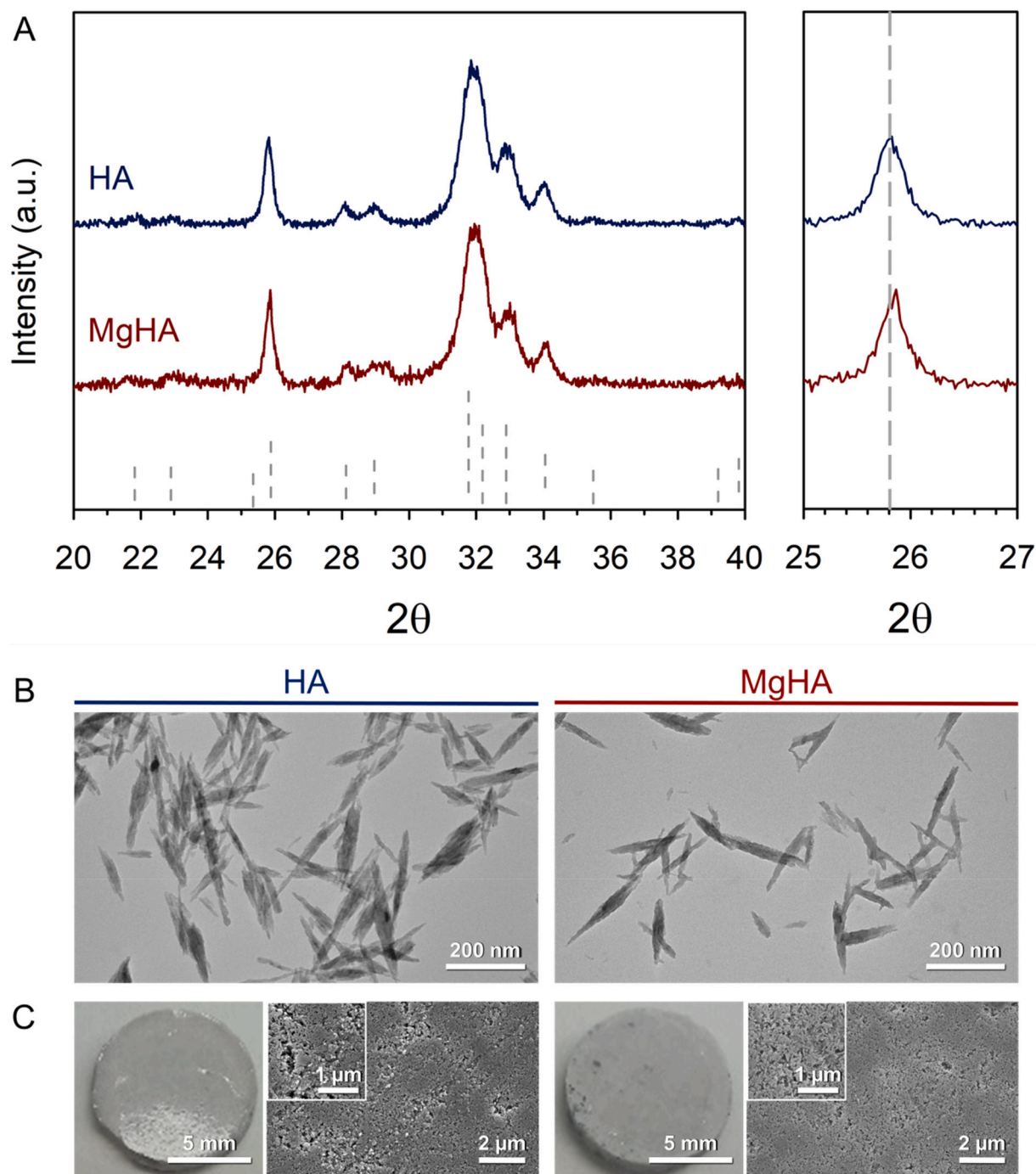
Fig. 1. Physicochemical characterisation of the synthesised HA NPs. (A) X-ray diffraction for the non-doped (HA) and magnesium-doped (MgHA) NPs. (B) TEM micrographs for both types of nanoparticles. (C) Images of the discs made of compacted HA and MgHA NPs. Insets with higher magnification of the SEM pictures showing the nanoparticles of the discs.

3.3. Nanoparticles – cell membrane interaction study

Any NPs internalisation process starts with the interaction of NPs with the cell membrane. Since the cell membrane is rich in receptors and some of them have a strong affinity for calcium, the adsorption of NPs on the cell membrane could potentially induce changes in cells. From a fundamental point of view, it is essential to disclose if the cytotoxic effect of the HA NPs comes mainly from their interaction with the cell membrane or is due to their internalisation inside the cells. Indeed, it has been reported that the toxicity of certain NPs (*e.g.* positively charged NPs) can derive from their reactivity when interfacing with the cellular

membrane [43]. For this purpose, cell culture studies were done either by supplementing HA NPs on the cells or by seeding cells on NPs-compacted discs. In these homogeneous discs, uptake of the nanoparticles into the cells is prevented and the interaction is limited to surface interaction with the cell membrane. In contrast, when the cells are exposed to the NPs suspended in the cell culture medium, both interactions are possible: not only the contact with the cell membrane but also their internalisation. In addition, the assay was done either with or without the supplementation of FBS in the cell culture medium to validate the direct interaction of the NPs with the cell membrane (FBS−) without the interference of adsorbed proteins, which are known to have
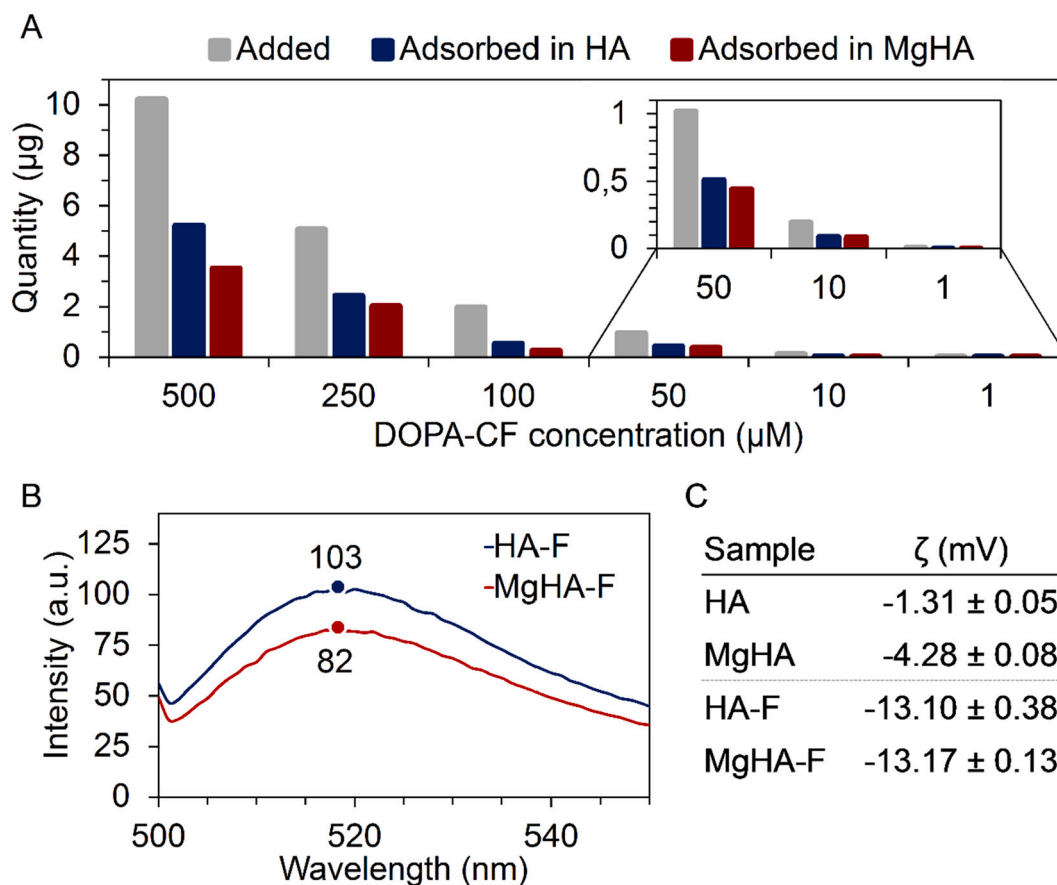
Fig. 2. Characterisation of the fluorescently functionalised NPs. (A) Adsorption of DOPA-CF peptide to HA and MgHA NPs at different initial concentrations. (B) Direct fluorescence intensity of the HA-F and MgHA-F NPs. (C) Zeta potential of the different materials.

a strong affinity for HA [44]. In general, these adsorbed proteins block the interaction of cellular receptors with the nanomaterial surface [45] causing a reduction in the cytotoxic effect due to a lower cell uptake [46].

Fig. 3A shows the morphology of the cells adhered to the samples imaged with acridine orange (AO) staining in the confocal microscope and by SEM. The well-spread morphology of the cells correlates to their viability when seeded on the discs – both in HA and MgHA –, similarly to the control condition (*i.e.* cells seeded on coverslips, without material), regardless of the removal of FBS. The cells on the discs of the serum-free samples presented minor difference in their morphology compared to the glass coverslip, exhibiting star-like shapes instead of elongated profiles, probably caused by the nature of the material. However, this difference was not relevant since the cells appeared perfectly attached to the discs' surfaces. SEM analysis of the surface morphology of the discs after incubation (Fig. S1 in the Supplementary Information) showed that the surface was almost unaltered, although some detachment of NPs could not be ruled out.

The results of the samples with the NPs suspensions demonstrated that the cells supplemented with both types of NPs in serum-containing medium presented no cytotoxicity. In contrast, in the absence of FBS, cells in contact with the suspension of HA or MgHA mostly died after 4 h, as observed by the drastic drop in cell population. Fig. 3B quantifies these findings by WST-1. The data obtained are consistent with the images, as cell death of 70 % for HA NPs suspension was revealed, whilst MgHA NPs presented a killing potential for 80 % of the cells, with statistically significant differences between the two conditions. In contrast, although a slight decrease in cell number was observed in HA FBS+ and in both types of discs in FBS− condition compared to the control, the differences were not statistically significant.

The higher cytotoxicity observed for MgHA NPs aligns with other studies in the literature, where the authors reported that doping HA NPs with small amounts of magnesium improved the cytotoxicity in MG-63, leaving mesenchymal stem cells alive [10]. However, HA NPs also showed high toxicity compared to MgHA NPs, which we believe is due to differences in the aggregation state of both types of NPs, as will be later discussed.

Regarding the differences observed in NPs suspension between FBS+ and FBS− conditions, several authors have demonstrated that the adsorption of proteins on the surface of HA NPs can strongly affect the adhesion properties to the cell membrane, reducing the uptake levels [45,46]. The reason for the reduced internalisation was explained by the electrostatic repulsion between the cell membrane and the negative charge that proteins confer to the HA NPs [10,47]. To circumvent this issue, it would be worthwhile to functionalise the NPs with cationic molecules to help in the process of internalisation in the presence of serum.

Overall, the results obtained suggest that the direct interaction of the cell surface with the material was not sufficient to cause cell death and it must be excluded as the main mechanism of cytotoxicity, being HA NPs internalisation a requirement for cell toxicity.

3.4. Investigation of nanoparticles internalisation

3.4.1. Flow cytometry assay

Flow cytometry (FC) has become an indispensable technique in cellular studies with nanomaterials. This method is based on high-throughput single-cell analysis, offering data that allow to understand the traffic of NPs inside the cells [48]. In order to monitor the nanoparticles' interaction with cells, a FC assay was performed using
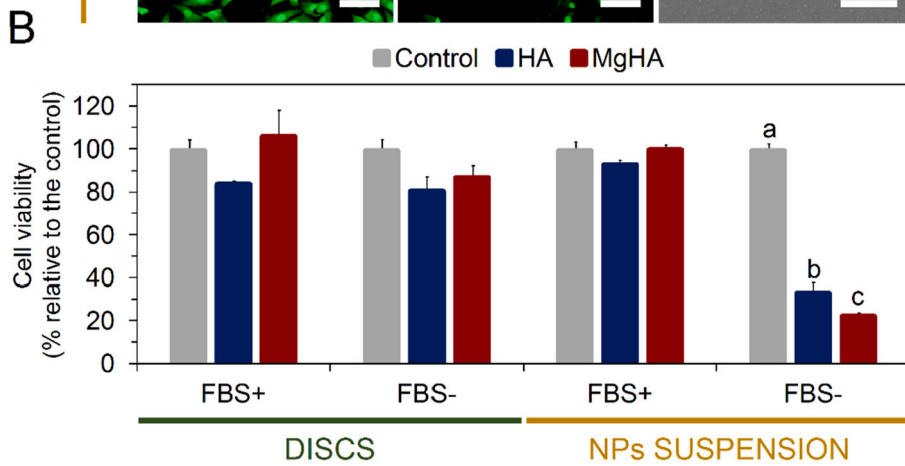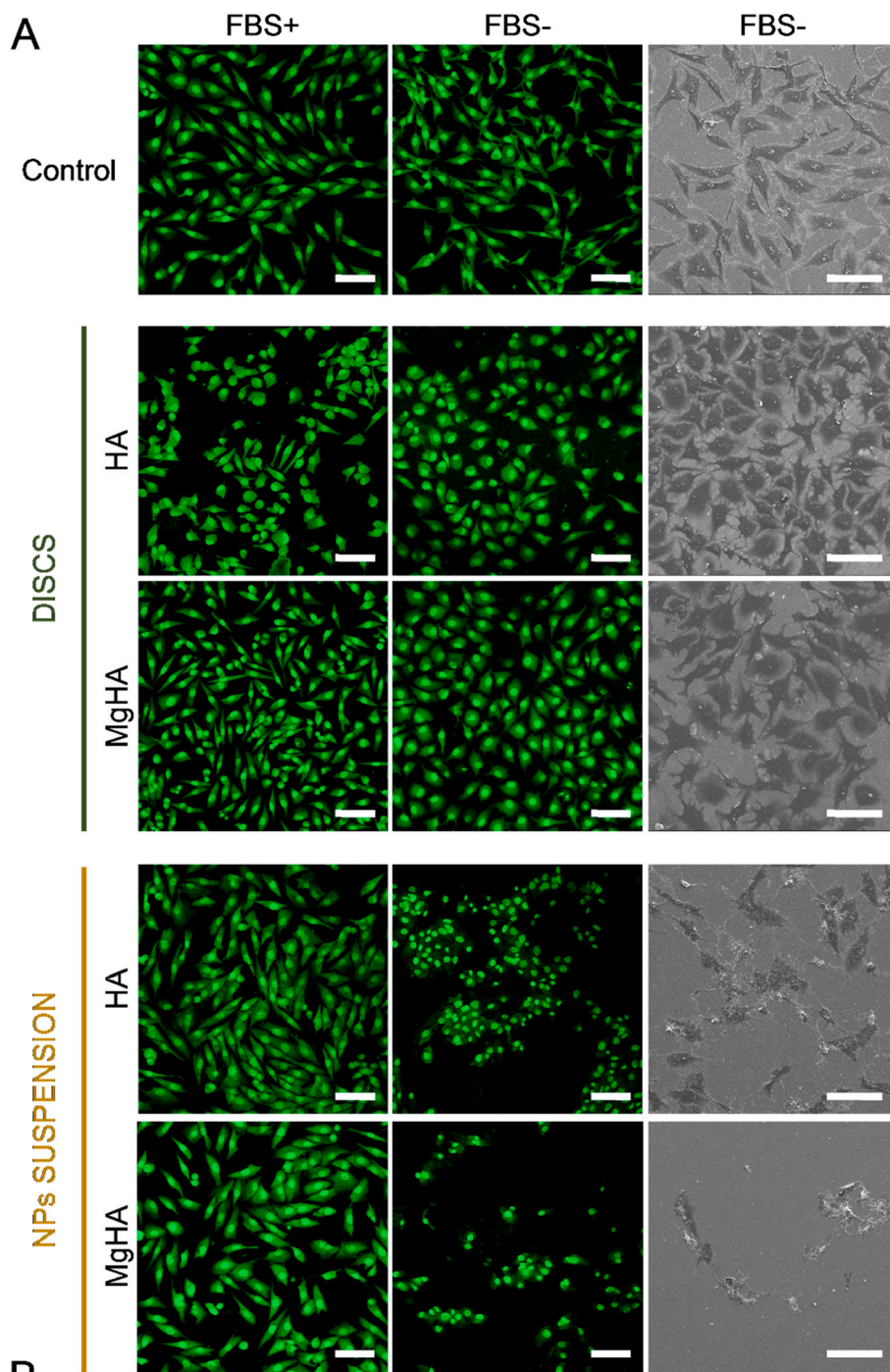
(caption on next page)

Fig. 3. Cytotoxicity assay comparing NPs compacted into discs and free NPs in suspension after 4 h of interaction with MG-63 cells. (A) Confocal microscopy visualisation of AO staining (first two columns) and SEM images (third column). Scale bars denote 100 μm. (B) Cell viability quantified using WST-1 reagent. Different letters in the graph (a, b, c) indicate statistically significant differences between samples ($n = 3$; p-value <0.05).

fluorescently labelled NPs (*i.e.* HA-F, MgHA-F) to track them in the cells. The results of non-doped NPs (HA-F) and magnesium-doped NPs (MgHA-F) are displayed in Fig. 4A and B, respectively. The threshold of the graphs was established from the analysis of negative controls (*i.e.* cells without the supplementation of fluorescent NPs). In addition, 10,000 events (*i.e.* cells) were analysed for all conditions, except for FBS− samples after 24 h incubation, where <1000 events were evaluated due to cell death.

At a first glance, the results from FC and cytotoxicity seemed to correlate well for the serum-free conditions (FBS−), since the high cytotoxicity observed from WST-1 (Fig. 3) paired with high percentages of cells associated with fluorescently labelled NPs, which is typically related to NPs internalisation. Indeed, 89.9 % of the cells at 4 h and 81.4 % at 6 h were fluorescently labelled with HA-F NPs in serum-free conditions. After 24 h the population of cells in the FC assay was too low, making the results less reliable. Although we did not use FC to evaluate cytotoxicity, the marked drop in cell population at 24 h clearly differed from the WST-1 assay, where 80 % of cell death was observed already at 4 h. We attribute this delay to the changes associated to the chemical binding of the DOPA-CF peptide on the surface of the NPs prior to the FC assay.

Analysing the behaviour of the HA-F NPs in serum-containing conditions (FBS+) it was observed a lower percentage of cells with labelled NPs at all the time points compared to the FBS− condition (Fig. 4A). However, there was a rather high percentage of cells with labelled NPs already at 4 h (*i.e.* 68.4 %) but no signs of cytotoxicity were detected by WST-1. This may indicate that the presence of serum proteins adsorbed on HA NPs modifies their uptake and degradation behaviour. However, one aspect that should not be overlooked to correctly interpret these results is that in all cell culture conditions except for MgHA NPs in FBS+, namely for HA-F FBS+/− and MgHA-F FBS−, the NPs tended to aggregate and sediment on top of the cells (Fig. 5). Upon sedimentation, the NPs could not be easily detached, indicating adhesion to the cell surface membrane. These results revealed that the detection of fluorescently labelled NPs in the FC studies cannot be solely associated to internalisation. NPs cannot only be present inside the cells (internalised), but also can remain attached to the external cell membrane. Moreover, this may apply to FBS− and FBS+ conditions. Thus, by FC it is not possible to distinguish where the NPs are located, and additional complementary techniques would be required to answer this question.

The results for the MgHA-F NPs exhibited an interesting behaviour (Fig. 4B). In serum-containing conditions (FBS+) a very low population of cells were stained by the NPs especially at 4 and 6 h, which aligned with the fact that in this condition NPs were well dispersed in the cell culture and NPs sedimentation did not occur. On the other hand, in serum-free conditions both NPs internalisation and NPs adhesion on the cell membrane took place simultaneously, which may complicate the interpretation of the results. However, it is clear that higher numbers of labelled cells were detected, especially at 6 h, which agreed with the high cytotoxicity observed by WST-1. The differences in terms of timing can be associated, as previously explained, with changes due to the fluorescent labelling of the NPs. As in the case of HA-F NPs, the reliability of the values at 24 h are compromised due to the low number of living cells at that time point.

To further understand the different outcomes obtained for HA-F and MgHA-F in FBS+ and FBS− conditions, cells with fluorescent NPs were imaged in a confocal microscope after being fixed and stained. The results illustrated in Fig. 5 clearly proved the sedimentation of NPs in serum-free media for both types of NPs (the green NPs were observed on the outer surface of the cell membrane, which was stained in red). In addition, the same tendency although to a lesser extent was observed for

HA-F NPs in FBS+ condition. Nevertheless, magnesium-doped nanoparticles presented a different behaviour, as they formed a stable colloidal suspension with the addition of FBS, avoiding their sedimentation on top of the cells. Although further studies would be necessary to find an explanation for this behaviour, we suspect that a combination of effects based on the nature of the protein corona adsorbed on the NPs and the ionic speciation surrounding the NPs, protects them from aggregation.

While stability studies of the NPs in cell culture media were not performed, we consistently observed by optical microscopy the sedimentation of NPs on top of the cells in all conditions (FBS− and FBS+), except for MgHA in serum-containing samples. As already mentioned, these findings agree with the FC results of MgHA in FBS+, which barely showed any sign of fluorescent NPs. Interestingly, the comparison of both types of NPs puts also forward that doping HA NPs may result in substantial changes in their properties (*e.g.* colloidal stability), which can affect, in turn, their adsorption and uptake behaviour. As previously said, understanding the colloidal stability of the suspensions is fundamental to better control the uptake of NPs by cells. In the work of Safi et al. the authors reported a strong NPs uptake that was related to the destabilization of the dispersions in the cell culture medium and their sedimentation on the cell membrane [49].

Overall, despite the robustness of the FC technique, it did not allow to differentiate internalised NPs from those attached to the surface of the cells. This calls for cautious analysis to avoid erroneous conclusions. Other authors have also highlighted the importance of differentiating membrane-bound NPs when using FC to quantify NPs internalisation and the danger when failing to do so [23].

Nonetheless, even being able to discriminate and quantify the real amount of NPs internalised, it would not be sufficient to predict their toxicity, as it has been previously demonstrated that the dissolution degree of the HA NPs is what eventually determines the toxicity. Therefore, the cytotoxicity does not only depend on the amount of NPs internalised but also on their crystallinity, specific surface area and composition, as well as on the cell type tested [50,51].

In light of this, the toxic effect of the HA NPs would be associated with the levels of calcium and phosphorus ions released in the cytosol after their dissolution: if the levels increase too much, it will induce cell death, whereas if the intracellular calcium levels remain low and sustained, cells will maintain their viability [18]. Therefore, a useful approach to predict cytotoxicity is to monitor intracellular calcium.

3.4.2. Intracellular calcium evaluation

As earlier mentioned, once the HA NPs enter in contact with the cellular membrane, the most common mechanism of internalisation is endocytosis, mostly by micropinocytosis [52]. Subsequently, the endosomes containing the NPs will fuse with lysosomes, which contain many acidic hydrolysing enzymes that decrease their pH to approximately 4.5. The most accepted hypothesis to explain the cytotoxic effect of the HA NPs is that HA is dissolved in these organelles, causing a notorious increase of calcium and phosphorus ions. The local accumulation of these ions can cause an osmotic pressure imbalance which can induce disruption of the lysosomes unless ions are pumped out sufficiently rapid to the cytosol. The cytotoxicity of HA NPs will depend on the levels of Ca^{2+} and P_i ions reaching the cytoplasm of the cell, where they can trigger programmed cell death or even necrosis [20,21].

To check this hypothesis, intracellular calcium markers are fundamental to help to quantify changes in the Ca^{2+} levels. In the present work, Fluo-4 AM probe was used for quantification, together with the corresponding imaging of calcium ions. Additionally, a positive apoptosis control was employed to distinguish between the increase of
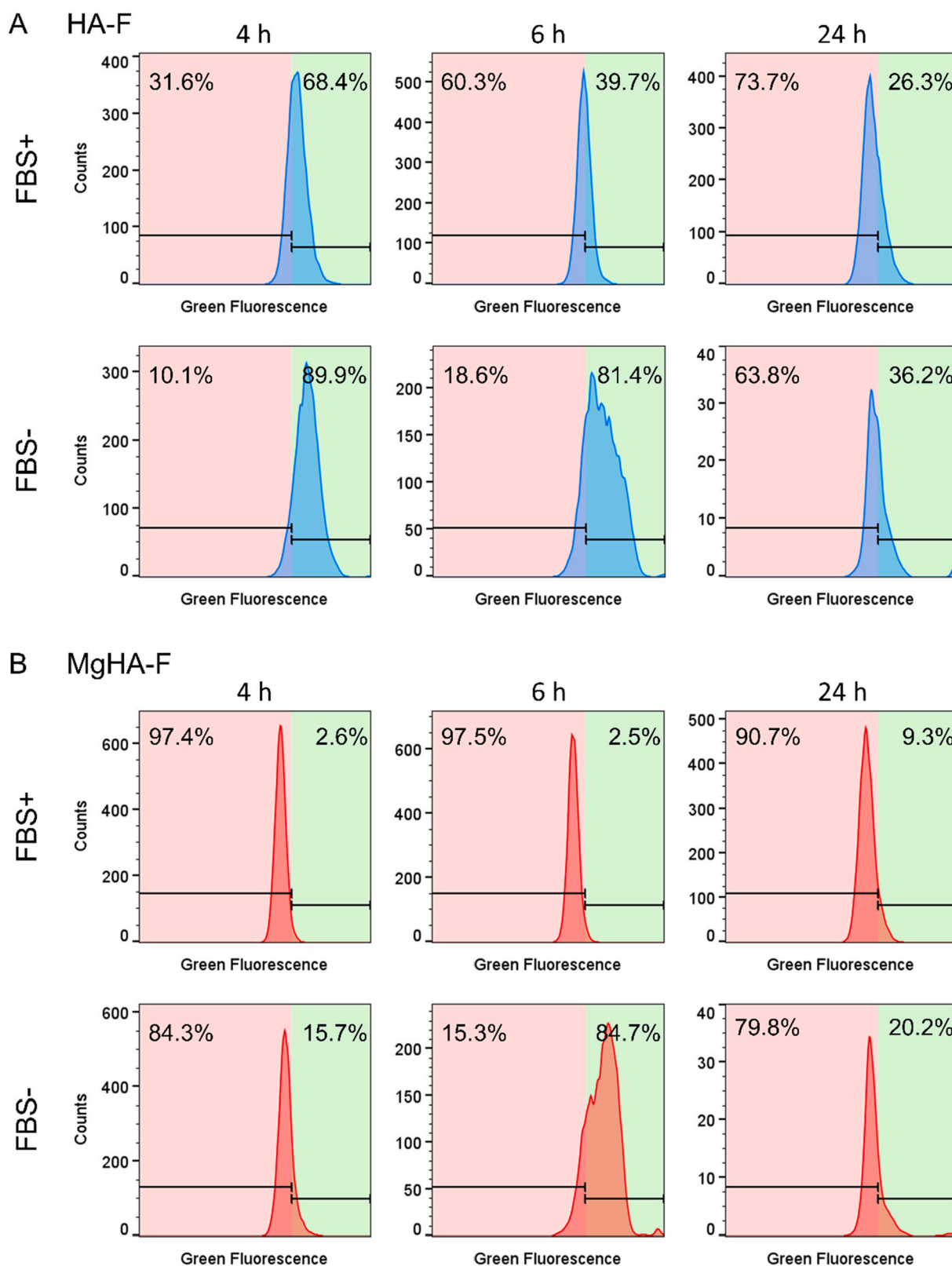
Fig. 4. Flow cytometry results of cells exposed to (A) HA-F and (B) MgHA-F for 4, 6 and 24 h. Histograms showing cell counts negatives (left, red-shadowed area) and positives (right, green-shadowed area) in green fluorescence. The threshold between positive and negative fluorescence was established from negative controls. In all cases, 10,000 events were analysed, except for the 24 h FBS− samples, where <1000 events were evaluated due to cell death.
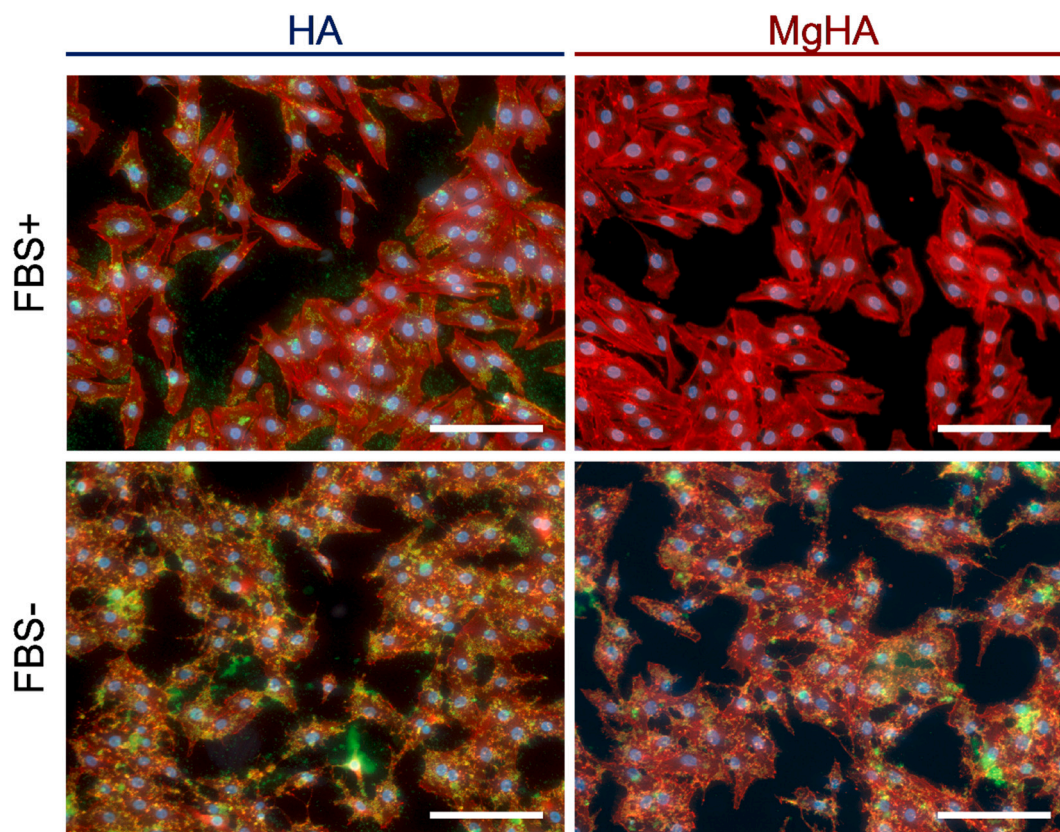
Fig. 5. Fluorescence images of MG-63 cells supplemented with HA-F and MgHA-F NPs for 4 h both in FBS+ and FBS− conditions. Red staining indicates actin filaments, blue dots denote cell nuclei and green intensity marks fluorescent nanoparticles. Scale bars represent 200 μm.

Ca^{2+} produced as part of the programmed cell death mechanism and the contribution of released ions after the dissolution of the NPs. Indeed, calcium, as a secondary messenger molecule, is highly involved in the signalling pathway of apoptosis [53].

Fig. 6A summarises the fluorescence intensity levels of Fluo-4 AM after 3 h of incubation of cells with the NPs, relative to the controls. The intracellular Ca^{2+} levels of the samples FBS+ were similar for all the conditions, with slightly higher fluorescence in the case of HA NPs. On the contrary, the fluorescence intensity of the samples supplemented with HA and MgHA in serum-free media dramatically rose to 4 times the values of the controls (*i.e.* control without NPs and apoptosis control). The significant increase in the levels of intracellular Ca^{2+} may be attributed to the contribution of dissolved HA NPs inside the lysosomes, as hypothesised. Moreover, the values obtained for the samples with FBS confirm the difficulty of the cells to uptake NPs when they are coated with a protein corona.

Images illustrating the calcium distribution in MG-63 cells are presented in Fig. 6B. Regardless of the addition of NPs, the cells exhibited similar appearance in all FBS+ conditions, showing homogenous staining throughout the cytosol. Interestingly, the cells of the apoptosis control (Fig. 6Bii) showed a singular morphology, exhibiting stressed fibres due to the nature of the sample (*i.e.* initial steps of the apoptotic process). In the serum-free condition, the control sample revealed homogeneous staining of cytosolic Ca^{2+}, similar to the serum-containing condition. In contrast, noticeable differences were observed for the other samples (*i.e.* HA, MgHA and apoptosis control, Figs. 6Bvi-viii), where Ca^{2+} was found concentrated in vesicles distributed all over the cytosol. Although several calcium-rich vesicles were observed in the control of apoptosis, the number of the vesicles was markedly higher for the nanoparticles-containing samples, indicating that the Ca^{2+} contribution mostly comes from the massive uptake of HA NPs. The presence of calcium-rich vesicles in the FBS− apoptosis sample may indicate the

membrane break of important intracellular calcium stores and the subsequent Fluo-4 permeability to them, caused by the advanced stage of the cell death process.

Various calcium stores are present in the cell, which could explain the selective staining of vesicles in Fig. 6. It is well established that the main intracellular calcium store is the endoplasmic reticulum (ER), together with the Golgi apparatus and mitochondria. However, there are other small-volume stores, such as acidocalcisomes, endosomes or lysosomes, dispersed throughout the cell that are considered as secondary Ca^{2+} stores [54,55]. Despite the classification in main and secondary Ca^{2+} stores, the concentration of calcium can reach comparable values between the lysosome lumen and the lumen of the ER [56]. As previously mentioned, Fluo-4 in all the serum-containing samples, as well as in the control FBS− exhibited homogeneous staining of the cytosol, proving that the fluorophore was not able to enter the ER, Golgi apparatus or mitochondria, as expected. Thus, it seems feasible that the small green-stained vesicles ranging from 0.3 to 0.6 μm in size observed could be attributed to intracellular Ca^{2+} localised in individual vesicular stores (*e.g.* lysosomes, endosomes, *etc.*) enriched by the presence of dissolved HA NPs. We expect these vesicles to have a compromised membrane to allow the entrance of the Fluo-4 molecule. It has to be noted that the fluorescence intensity for the serum-free samples loaded with NPs had to be decreased during the analysis to avoid the saturation of the vesicles. This adjustment reduced the overall fluorescence and masked the contribution of cytosolic calcium, that could be observed before this modification. Hence, the selective staining of calcium-rich vesicles does not exclude an increase in cytosolic Ca^{2+}, which would be responsible for the cytotoxicity. Unfortunately, the results reported by other authors on intracellular calcium determination does not discriminate between free cytosolic Ca^{2+} from Ca^{2+} retained in vesicles. This is for instance the case of the studies that rely on the quantification of fluorescence intensity by microplate reader or by FC [21,24].
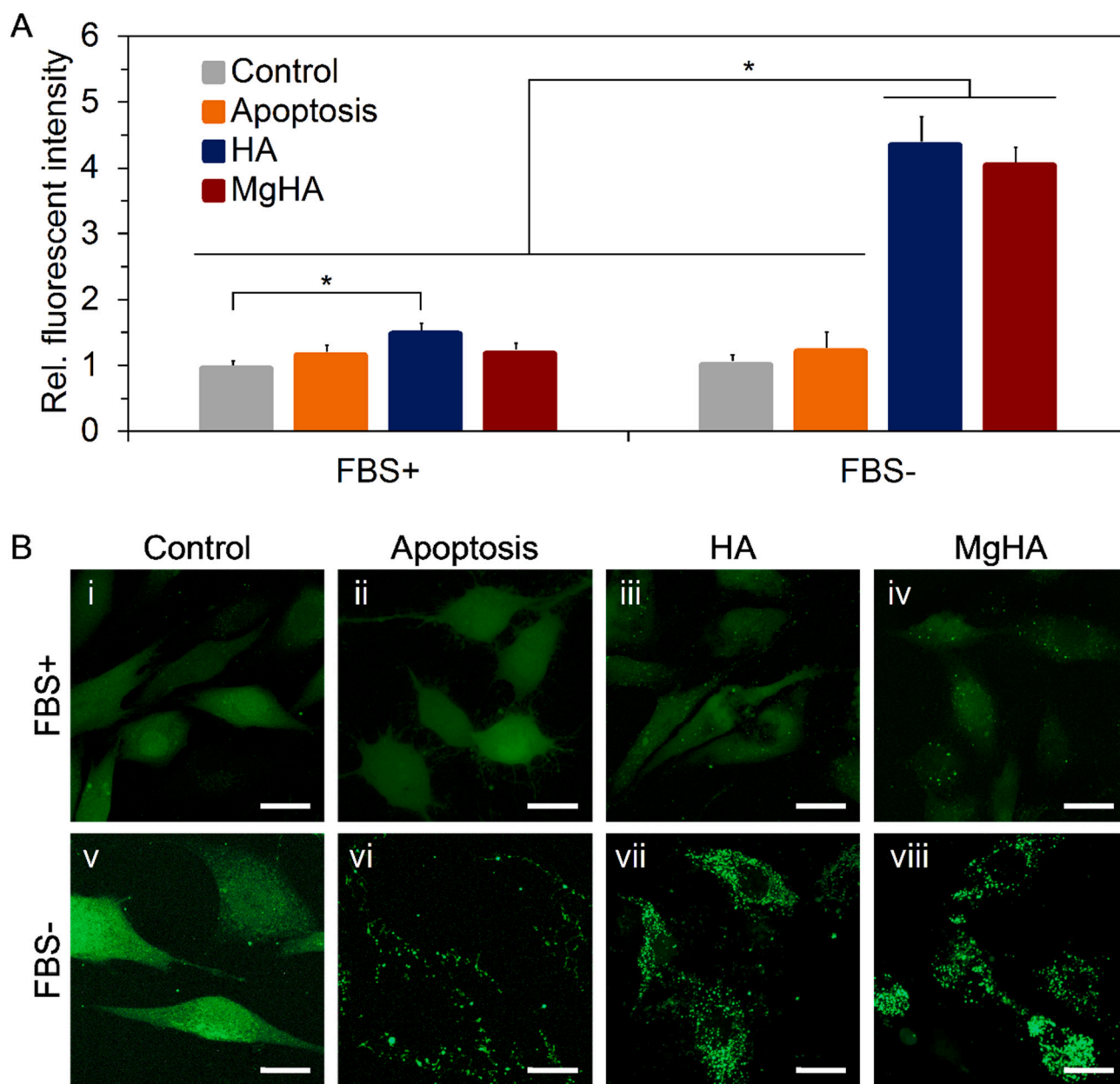
Fig. 6. Intracellular calcium evaluation of cells exposed to the NPs for 3 h and stained with Fluo-4 AM. An apoptosis control was also studied. (A) Intracellular calcium quantified in a fluorescence microplate reader. (B) Intracellular calcium imaged by fluorescence confocal microscopy. Scale bars represent 20 μm. * indicates statistically significant differences ($n = 4$; p-value <0.05).

The observation of such stained vesicles has been sometimes attributed to subcellular compartmentalisation [57]. Even though we demonstrate the absence of these highly fluorescent vesicles in the control samples and in all the serum-supplemented conditions, which clearly discarded this possibility, further analysis has to be done in order to confirm the presence and determine the composition of the vesicles.

3.4.3. Transmission electron microscopy and cryo-soft X-ray tomography

Transmission electron microscopy (TEM) and cryo-soft X-ray tomography (cryo-SXT) were performed in selected specimens (*i.e.* serum-free samples) to check the uptake of NPs and to assess the distribution of calcium-rich vesicles inside the cells. TEM, as a high-resolution technique, with resolution below 5 nm, is typically used to evaluate the internalisation of nanomaterials. In contrast, cryo-SXT is a novel technique that uses X-ray to image frozen pristine samples in the water window region (*i.e.* between the carbon K edge at 284 eV and the oxygen K edge at 543 eV) with resolution about 25 to 40 nm. Within this region, X-rays are absorbed an order of magnitude more strongly by carbon- and nitrogen-containing organic material than by water, allowing direct visualisation of the cellular structures while water remains nearly transparent [58,59]. Thus, comparing both techniques, while TEM has the advantage of resolution, it requires major processing steps such as fixing, dehydration and slicing to observe the samples. All along these steps, electrolytes and low molecular weight organic compounds can potentially be washed out from the cells and any information concerning the presence of ionic soluble content will be missed [54]. In addition, artefacts can be easily introduced during sample processing. Instead, cryo-SXT has lower resolution than TEM but enables mesoscale imaging of the whole cellular ultrastructure without any processing other than vitrification [60,61]. Thus, the possibility to image cells under near-native conditions is a strong asset of this technique. Moreover, cryo-SXT offers the possibility to quantify the results and distinguish
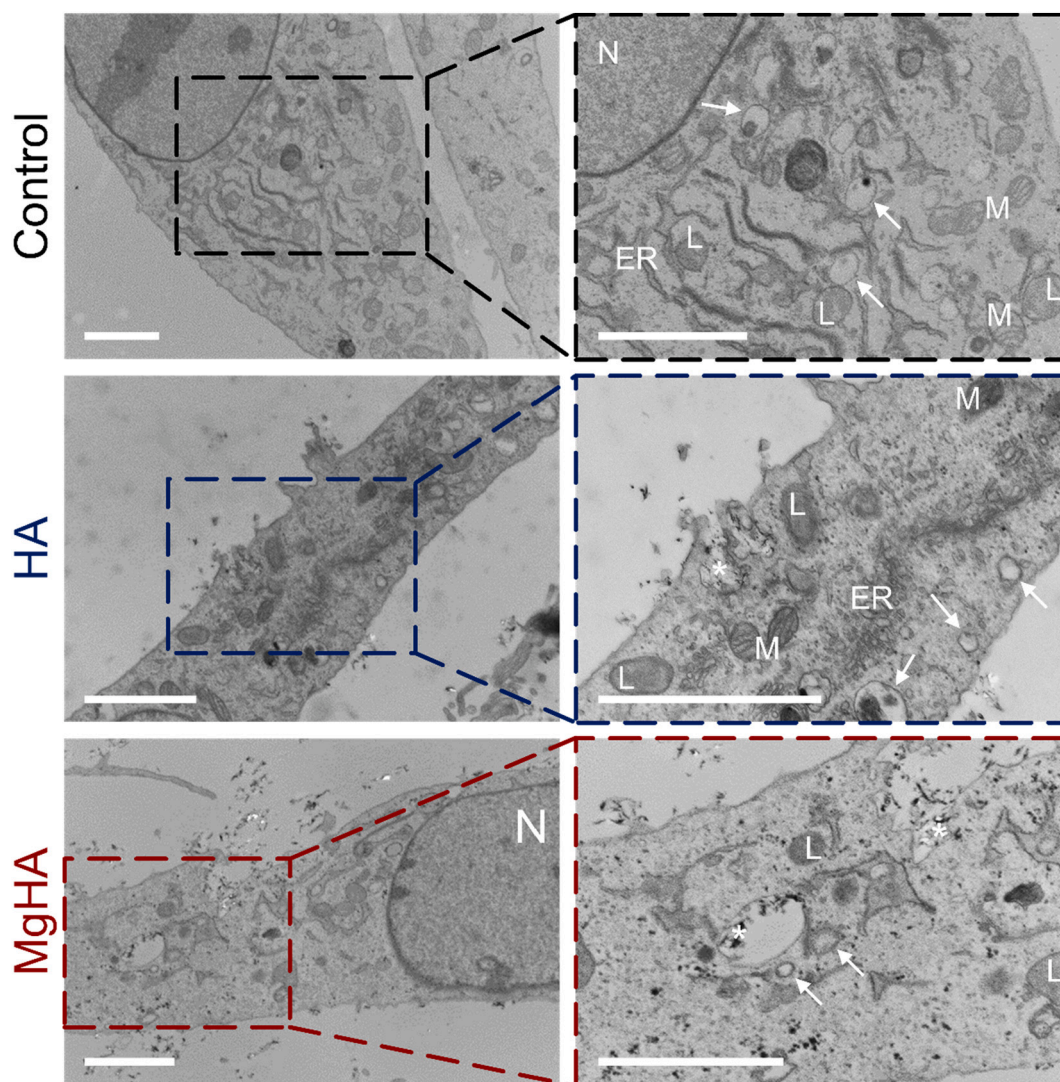
Fig. 7. TEM images of cells without the addition of nanomaterials (control) and after the supplementation of HA and MgHA NPs in serum-free conditions. * indicates NPs. ER, L and M stand for endoplasmic reticulum, lysosomes and mitochondria, respectively. White arrows point vesicles (either empty or with residual content). Scale bars denote 2 μm.

cellular structures based on linear absorption coefficients, following the Beer-Lambert law [58,62].

With respect to the TEM results, illustrated in Fig. 7, samples of cells supplemented with HA and MgHA NPs in serum-free conditions were examined, together with a control without NPs. The results not only confirmed the uptake of nanoparticles in both supplemented samples, but they also denoted the absence of electrodense vesicles comparable in size to the ones observed by confocal fluorescence microscopy. Instead, other vesicles (either empty or with residual content) were seen, which was consistent with the idea that electrolytes such as Ca^{2+} and P_i were lost during sample processing. However, it was impossible to know the original composition of these organelles using this technique.

In contrast, cryo-SXT revealed interesting differences compared to TEM. Fig. 8 shows the X-ray projection images that provide an overview of the cell of interest (8i and iv), together with relevant tomographic sections taken from the tilt series (8ii and v) and their segmentation (8iii and vi). Videos of the whole aligned tilt series can be found in the Electronic Supplementary Material. In the selected sections, small highly absorbing vesicles of around 0.3 to 0.6 μm and reaching up to 1 μm were readily visible. Similar-looking vesicles have been ascribed by other authors as lipid droplets (LDs), due to their small size and their high carbon content that highly absorbs at 520 eV [63]. However, LDs are

usually described as fully dense dark vesicles by cryo-SXT or, in some cases, as vesicles containing one lighter vesicle within [58]. Furthermore, three different components of the endocytic pathway can be distinguished. First, early endosomes that can be considered as sorting vesicles and are agreed to appear as membrane-bound organelles with a relatively uniform interior by cryo-SXT. Multivesicular bodies (MVBs), formed from early endosomes by the invagination of the membrane into their own lumen, which, imaged by cryo-SXT, should clearly contain one or more internal lighter vesicles. And lysosomes, the last organelle of the endocytic pathway that break down biomolecules into simple compounds thanks to many hydrolytic enzymes, and typically show an electrodense lumen with internal granular structures [58,63,64]. In this regard, Fig. 8v shows that most electrodense vesicles contained >2 low-absorbing vesicles, which suggested the presence of endocytic vesicles rather than LDs and, more specifically, of MVBs. Actually, MVBs are organelles formed by the maturation of early endosomes. They are also known as late endosomes and are always identified in the degradation pathway of any endocytic process [65]. In the case of Fig. 8ii, a lower density of MVB vesicles was observed along with larger grainy structures compatible with lysosomes or endolysosomes, as well as a large vesicle containing pristine HA NPs. In general, the large number of the darker MVBs would match with the green-stained vesicles observed by
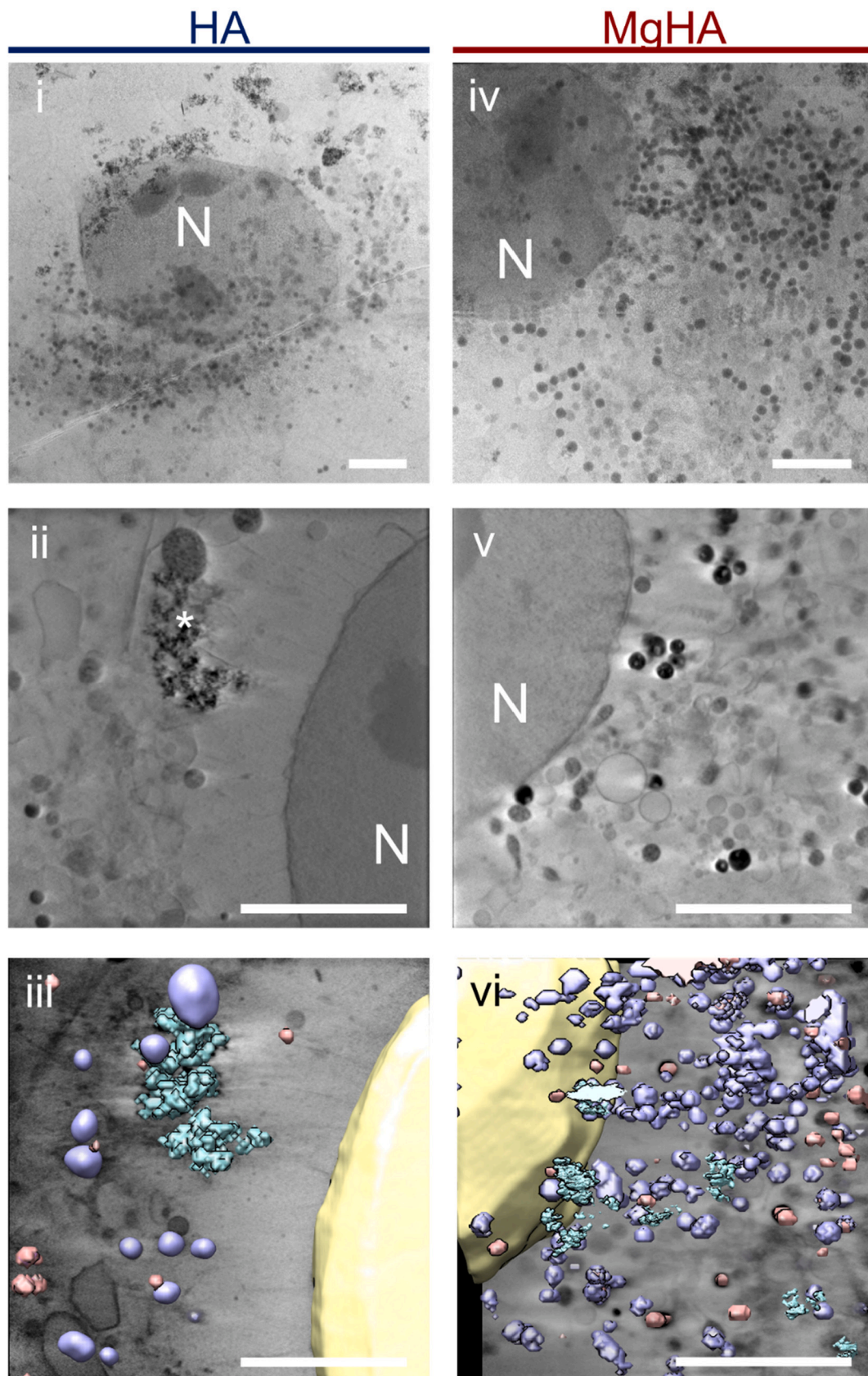
Fig. 8. Cryo-SXT of cells after 3 h of exposure to HA and MgHA NPs. i and iv showing mosaic projections, ii and v display relevant tomographic sections, and iii and vi reveal the segmentation of the same stacked tomograms. N denotes nuclei and * stands for internalised NPs. Nuclei are segmented in yellow, lipid droplets in pink, nanoparticles in blue and multivesicular bodies in purple. Scale bar represents 5 μm.

fluorescence confocal microscopy (Fig. 6B). However, distinguishing LDs from MVBs is not so straightforward.

Apart from discrimination of the different organelles by visual inspection, cryo-SXT allows quantitative determination of the linear absorption coefficient (LAC) for each cellular component [59,66] (Table 2). Therefore, in order to better elucidate the nature of these small vesicles, the selected tilt series were segmented and their LACs quantified. Nuclei (segmented in yellow) resulted in a LAC of 0.29 ± 0.02 μm^{-1}, while internalised NPs presented a high LAC value of 1.94 ± 0.02 μm^{-1}. In addition, two different vesicles were identified: LDs with a LAC of 1.42 ± 0.03 μm^{-1}, and MVBs with a LAC value of 1.09 ± 0.05 μm^{-1}. It is worth noting that the standard deviation obtained for these values is very low, and this indicates the high similarity of LACs between both sample conditions. The differences in LAC values between LD and MVB proved compositional differences between both types of vesicles. Thus, based on LAC values we could unambiguously map MVBs and LDs from the analysed cells (Fig. 8iii and vi). It is known that LD is typically the structure with the highest LAC value due to its increased carbon content compared to the other organelles, which agrees with the results obtained (LAC of LDs was 1.42 μm^{-1} *vs.* LAC of nuclei 0.29 μm^{-1}). The fact that cells with internalised NPs contained MVBs with LAC values close to the LD ones, implies that these vesicles should contain highly absorbing elements. In combination with the very high LAC value of the solid NPs, it indicates that the electrodense vesicles may contain degraded NPs. Accordingly, these results suggest that the Ca^{2+}-rich vesicles identified by confocal microscopy, should not be considered as artefacts and they likely correspond to MVBs.

Moreover, although both samples had Ca-rich vesicles with similar LACs (*i.e.* 1.11 ± 0.03 μm^{-1} and 1.07 ± 0.04 μm^{-1} for HA and MgHA, respectively), the segmentation revealed different size and distribution of these vesicles. Specifically, HA presented a lower amount of vesicles but of larger dimensions, whilst the vesicles in MgHA were smaller but present in higher quantity. Analysis of the tomograms obtained for the cell exposed to HA NPs showed the capture of a less advanced degradation state of the NPs, which together with the tomogram of the cell exposed to MgHA allows to see the evolution of the degradation of these materials.

An additional aspect to explore in the future from cryo-SXT is cryospectroscopic imaging by changing the imaging energy from 520 eV. In a recent work by Gal et al. the authors set the energy to 353 eV, which is the absorbing energy for Ca, to investigate the distribution of calcium-containing organelles in calcifying and non-calcifying species in algae [26]. A very distinct Ca^{2+} map was shown, proving to be a powerful tool to trace calcium stores in pristine conditions. This technique applied to our samples would allow gaining further insights in the quantification and distribution of intracellular calcium.

The study of intracellular calcium is of major relevance when trying to elucidate the fate of internalised NPs, as changes in the cytosolic calcium of the cells help to understand the cytotoxicity caused by HA NPs. Through the combination of different techniques, both conventional and advanced, we have been able to detect the presence of multiple MVBs which potentially carry degraded NPs. However, discrimination of these Ca-rich stores from cytosolic calcium would be needed to better assess toxicity. We have demonstrated the limitations of various techniques in this regard, but also the great potential of intracellular calcium probes combined with cryo-SXT.

4. Conclusions

The main goal of this work was to understand and to prove the cytotoxic mechanism of hydroxyapatite NPs using the common techniques in the field together with cryo-SXT imaging at the ALBA synchrotron. The studies revealed the internalisation of HA and MgHA NPs as the main toxicity mechanism, with minor contribution coming from the material interaction with the outer cell surface. It was noticed that the results from FC when applied to investigate the uptake of NPs need

Table 2
Linear absorption coefficient (LAC) of the different cellular components.

	Nucleus (μm^{-1})	Nanoparticles (μm^{-1})	Lipid droplets (μm^{-1})	Multivesicular bodies (μm^{-1})
	Yellow	Blue	Pink	Purple
HA	0.29 ± 0.02	1.94 ± 0.02	1.42 ± 0.03	1.11 ± 0.03
MgHA				1.07 ± 0.04

to be carefully analysed, as the contribution of the NPs attached to the cell membrane can induce to wrong conclusions. The use of intracellular calcium probes revealed increased levels in the calcium content of the samples supplemented with NPs. The major contribution to the intracellular calcium was from the staining of a high number of small calcium-rich vesicles. The results from cryo-SXT proved that these vesicles were MVBs and not a staining artefact. Despite the high resolution of TEM, dehydration of the sample impeded the study of these vesicles due to their liquid content. Overall, the combination of calcium-fluorescent probes together with cryo-SXT provided the best tools to investigate intracellular calcium of cells with internalised HA and MgHA NPs.

Supplementary data to this article can be found online at https://doi.org/10.1016/j.bioadv.2022.213148.

CRediT authorship contribution statement

Declaration of competing interest

The authors declare that they have no known competing financial interests or personal relationships that could have appeared to influence the work reported in this paper.

Data availability

No data was used for the research described in the article.

Acknowledgements

References

[1] S. Mondal, G. Hoang, P. Manivasagan, M.S. Moorthy, T.P. Nguyen, T.T. Vy Phan, H. H. Kim, M.H. Kim, S.Y. Nam, J. Oh, Nano-hydroxyapatite bioactive glass composite

scaffold with enhanced mechanical and biological performance for tissue engineering application, Ceram. Int. 44 (2018) 15735–15746, https://doi.org/10.1016/j.ceramint.2018.05.248.

[2] S. Mondal, G. Hoang, P. Manivasagan, M.S. Moorthy, T.T. Vy Phan, H.H. Kim, T. P. Nguyen, J. Oh, Rapid microwave-assisted synthesis of gold loaded hydroxyapatite collagen nano-bio materials for drug delivery and tissue engineering application, Ceram. Int. 45 (2019) 2977–2988, https://doi.org/10.1016/j.ceramint.2018.10.016.

[3] Q. Wang, J. Yan, J. Yang, B. Li, Nanomaterials promise better bone repair, Mater. Today 19 (2016) 451–463, https://doi.org/10.1016/j.mattod.2015.12.003.

[4] T.N.T. Do, W.-H. Lee, C.-Y. Loo, A.V. Zavgorodniy, R. Rohanizadeh, Hydroxyapatite nanoparticles as vectors for gene delivery, Ther. Deliv. 3 (2012) 623–632. http://www.ncbi.nlm.nih.gov/pubmed/22834406.

[5] Z.-S. Liu, S.-L. Tang, Z.-L. Ai, Effects of hydroxyapatite nanoparticles on proliferation and apoptosis of human hepatoma BEL-7402 cells, World J. Gastroenterol. 9 (2003) 1968–1971, https://doi.org/10.3748/wjg.v9.i9.1968.

[6] J. Hu, Z.-S. Liu, S.-L. Tang, Y.-M. He, Effect of hydroxyapatite nanoparticles on the growth and p53/c-myc protein expression of implanted hepatic VX 2 tumor in rabbits by intravenous injection, World J. Gastroenterol. 13 (2007), https://doi.org/10.3748/wjg.v13.i20.2798, 2798-2082.

[7] S.-H. Chu, D.-F. Feng, Y.-B. Ma, Z.-Q. Li, Hydroxyapatite nanoparticles inhibit the growth of human glioma cells in vitro and in vivo, Int. J. Nanomedicine 7 (2012) 3659–3666, https://doi.org/10.2147/IJN.S33584.

[8] F. Qing, Z. Wang, Y. Hong, M. Liu, B. Guo, H. Luo, X. Zhang, Selective effects of hydroxyapatite nanoparticles on osteosarcoma cells and osteoblasts, J. Mater. Sci. Mater. Med. 23 (2012) 2245–2251, https://doi.org/10.1007/s10856-012-4703-6.

[9] S. Dey, M. Das, V.K. Balla, Effect of hydroxyapatite particle size, morphology and crystallinity on proliferation of colon cancer HCT116 cells, Mater. Sci. Eng. C 39 (2014) 336–339, https://doi.org/10.1016/j.msec.2014.03.022.

[10] Z. Zhao, M. Espanol, J. Guillem-Marti, D. Kempf, A. Diez-Escudero, M.-P. Ginebra, Ion-doping as a strategy to modulate hydroxyapatite nanoparticle internalization, Nanoscale 8 (2016) 1595–1607, https://doi.org/10.1039/C5NR05262A.

[11] A. Guilbert, M. Gautier, I. Dhennin-Duthille, N. Haren, H. Sevestre, H. Ouadid-Ahidouch, Evidence that TRPM7 is required for breast cancer cell proliferation, Am. J. Physiol. Cell Physiol. 297 (2009) C493–C502, https://doi.org/10.1152/ajpcell.00624.2008.

[12] I. Dhennin-Duthille, M. Gautier, M. Faouzi, A. Guilbert, M. Brevet, D. Vaudry, A. Ahidouch, H. Sevestre, H. Ouadid-Ahidouch, High expression of transient receptor potential channels in human breast cancer epithelial cells and tissues: correlation with pathological parameters, Cell. Physiol. Biochem. 28 (2011) 813–822, https://doi.org/10.1159/000335795.

[13] P. Rybarczyk, M. Gautier, F. Hague, I. Dhennin-Duthille, D. Chatelain, J. Kerr-Conte, F. Pattou, J.-M. Regimbeau, H. Sevestre, H. Ouadid-Ahidouch, Transient receptor potential melastatin-related 7 channel is overexpressed in human pancreatic ductal adenocarcinomas and regulates human pancreatic cancer cell migration, Int. J. Cancer 131 (2012) E851–E861, https://doi.org/10.1002/ijc.27487.

[14] E. Abed, R. Moreau, Importance of melastatin-like transient receptor potential 7 and cations (magnesium, calcium) in human osteoblast-like cell proliferation, Cell Prolif. 40 (2007) 849–865, https://doi.org/10.1111/j.1365-2184.2007.00476.x.

[15] L.Y. He, X.M. Zhang, B. Liu, Y. Tian, W.H. Ma, Effect of magnesium ion on human osteoblast activity, Braz. J. Med. Biol. Res. 49 (2016) 1–6, https://doi.org/10.1590/1414-431X20165257.

[16] M.B.J. Safi, J. Courtois, M. Seigneuret, H. Conjeaud, The effects of aggregation and protein corona on the cellular internalization of iron oxide nanoparticles, Biomaterials 32 (2011) 9353–9363.

[17] M. Motskin, D.M. Wright, K. Muller, N. Kyle, T.G. Gard, A.E. Porter, J.N. Skepper, Hydroxyapatite nano and microparticles: correlation of particle properties with cytotoxicity and biostability, Biomaterials 30 (2009) 3307–3317, https://doi.org/10.1016/j.biomaterials.2009.02.044.

[18] S. Neumann, A. Kovtun, I.D. Dietzel, M. Epple, R. Heumann, The use of size-defined DNA-functionalized calcium phosphate nanoparticles to minimise intracellular calcium disturbance during transfection, Biomaterials 30 (2009) 6794–6802, https://doi.org/10.1016/j.biomaterials.2009.08.043.

[19] Y. Wang, J. Wang, H. Hao, M. Cai, S. Wang, J. Ma, Y. Li, C. Mao, S. Zhang, In vitro and in vivo mechanism of bone tumor inhibition by selenium-doped bone mineral nanoparticles, ACS Nano (2016), https://doi.org/10.1021/acsnano.6b03835 acsnano.6b03835.

[20] Z. Liu, Y. Xiao, W. Chen, Y. Wang, B. Wang, G. Wang, X. Xu, R. Tang, Calcium phosphate nanoparticles primarily induce cell necrosis through lysosomal rupture: the origination of material cytotoxicity, J. Mater. Chem. B 2 (2014) 3480, https://doi.org/10.1039/c4tb00056k.

[21] L.-H. Huang, X.-Y. Sun, J.-M. Ouyang, Shape-dependent toxicity and mineralization of hydroxyapatite nanoparticles in A7R5 aortic smooth muscle cells, Sci. Rep. 9 (2019) 18979, https://doi.org/10.1038/s41598-019-55428-9.

[22] E.C. Cho, J. Xie, P.A. Wurm, Y. Xia, Understanding the role of surface charges in cellular adsorption versus internalization by selectively removing gold nanoparticles on the cell surface with a I 2/KI etchant, Nano Lett. 9 (2009) 1080–1084, https://doi.org/10.1021/nl803487r.

[23] G.B. Braun, T. Friman, H.-B. Pang, A. Pallaoro, T.H. de Mendoza, A.-M. A. Willmore, V.R. Kotamraju, A.P. Mann, Z.-G. She, K.N. Sugahara, N.O. Reich, T. Teesalu, E. Ruoslahti, Etchable plasmonic nanoparticle probes to image and quantify cellular internalization, Nat. Mater. 13 (2014) 904–911, https://doi.org/10.1016/j.physbeh.2017.03.040.

[24] W. Tang, Y. Yuan, C. Liu, Y. Wu, X. Lu, J. Qian, Differential cytotoxicity and particle action of hydroxyapatite nanoparticles in human cancer cells, Nanomedicine 9 (2014) 397–412, https://doi.org/10.2217/nnm.12.217.

[25] A. Takahashi, P. Camacho, J.D. Lechleiter, B. Herman, Measurement of intracellular calcium, Physiol. Rev. 79 (1999) 1089–1125, https://doi.org/10.1016/S1385-299X(00)00003-9.

[26] A. Gal, A. Sorrentino, K. Kahil, E. Pereiro, D. Faivre, A. Scheffel, Native-state imaging of calcifying and noncalcifying microalgae reveals similarities in their calcium storage organelles, Proc. Natl. Acad. Sci. U. S. A. 115 (2018) 11000–11005, https://doi.org/10.1073/pnas.1804139115.

[27] A. Sorrentino, E. Malucelli, F. Rossi, C. Cappadone, G. Farruggia, C. Moscheni, A. J. Perez-Berna, J.J. Conesa, C. Colletti, N. Roveri, Calcite as a precursor of hydroxyapatite in the early biomineralization of differentiating human bone-marrow mesenchymal stem cells _ enhanced reader.Pdf, Int. J. Mol. Sci. 22 (2021) 4939, https://doi.org/10.3390/ijms22094939.

[28] A. Procopio, E. Malucelli, A. Pacureanu, C. Cappadone, G. Farruggia, A. Sargenti, S. Castiglioni, D. Altamura, A. Sorrentino, C. Giannini, E. Pereiro, P. Cloetens, J.A. M. Maier, S. Iotti, Chemical fingerprint of zn-hydroxyapatite in the early stages of osteogenic differentiation, ACS Cent. Sci. 5 (2019) 1449–1460, https://doi.org/10.1021/acscentsci.9b00509.

[29] M. Šupová, T. Suchý, Z. Sucharda, E. Filová, J.N.L.M. der Kinderen, M. Steinerová, L. Bačáková, G.S. Martynková, The comprehensive in vitro evaluation of eight different calcium phosphates: significant parameters for cell behavior, J. Am. Ceram. Soc. 102 (2019) 2882–2904, https://doi.org/10.1111/jace.16110.

[30] M. Epple, Review of potential health risks associated with nanoscopic calcium phosphate, Acta Biomater. 77 (2018) 1–14, https://doi.org/10.1016/j.actbio.2018.07.036.

[31] J. Gustavsson, M.-P. Ginebra, J.A. Planell, E. Engel, Osteoblast-like cellular response to dynamic changes in the ionic extracellular environment produced by calcium-deficient hydroxyapatite, J. Mater. Sci. Mater. Med. 23 (2012) 2509–2520, https://doi.org/10.1007/s10856-012-4705-4.

[32] J.-M. Sadowska, J. Guillem-Marti, E.B. Montufar, M. Espanol, M.-P. Ginebra, Biomimetic versus sintered calcium phosphates: the in vitro behavior of osteoblasts and mesenchymal stem cells, Tissue Eng. Part A 23 (2017) 1297–1309, https://doi.org/10.1089/ten.tea.2016.0406.

[33] J.M. Sadowska, J. Guillem-Marti, M. Espanol, C. Stähli, N. Döbelin, M.P. Ginebra, In vitro response of mesenchymal stem cells to biomimetic hydroxyapatite substrates: a new strategy to assess the effect of ion exchange, Acta Biomater. 76 (2018) 319–332, https://doi.org/10.1016/j.actbio.2018.06.025.

[34] P.Kord Forooshani, B.P. Lee, Recent approaches in designing bioadhesive materials inspired by mussel adhesive protein, J. Polym. Sci. A Polym. Chem. 55 (2017) 9–33, https://doi.org/10.1002/pola.28368.

[35] L. Oliver-Cervelló, H. Martin-Gómez, L. Reyes, F. Noureddine, E. Ada Cavalcanti-Adam, M. Ginebra, C. Mas-Moruno, An engineered biomimetic peptide regulates cell behavior by synergistic integrin and growth factor signaling, Adv. Healthc. Mater. 10 (2021), 2001757, https://doi.org/10.1002/adhm.202001757.

[36] J. Otón, E. Pereiro, A.J. Pérez-Berná, L. Millach, C.O.S. Sorzano, R. Marabini, J. M. Carazo, Characterization of transfer function, resolution and depth of field of a soft X-ray microscope applied to tomography enhancement by wiener deconvolution, Biomed. Opt. Express. 7 (2016) 5092, https://doi.org/10.1364/BOE.7.005092.

[37] J.R. Kremer, D.N. Mastronarde, J.R. McIntosh, Computer visualization of three-dimensional image data using IMOD, J. Struct. Biol. 116 (1996) 71–76, https://doi.org/10.1006/jsbi.1996.0013.

[38] R. Gordon, R. Bender, G.T. Herman, Algebraic reconstruction techniques (ART) for three-dimensional electron microscopy and X-ray photography, J. Theor. Biol. 29 (1970) 471–481, https://doi.org/10.1016/0022-5193(70)90109-8.

[39] S. Diallo-garcia, D. Laurencin, J. Kra, S. Casale, M.E. Smith, Influence of magnesium substitution on the basic properties of hydroxyapatites, J. Phys. Chem. C (2011) 24317–24327.

[40] W.M. Chirdon, W.J. O'Brien, R.E. Robertson, Adsorption of catechol and comparative solutes on hydroxyapatite, J. Biomed. Mater. Res. 66B (2003) 532–538, https://doi.org/10.1002/jbm.b.10041.

[41] H.S. Yang, J. Park, W.G. La, H.-K. Jang, M. Lee, 3,4-dihydroxyphenylalanine-assisted hydroxyapatite nanoparticle coating on polymer scaffolds for efficient osteoconduction, Tissue Eng. Part C 18 (2012) 245–251, https://doi.org/10.1089/ten.tec.2011.0373.

[42] V. Ozhukil Kollath, S. Mullens, J. Luyten, K. Traina, R. Cloots, Effect of DOPA and dopamine coupling on protein loading of hydroxyapatite, Mater. Technol. 31 (2016) 241–245, https://doi.org/10.1179/1753555715Y.0000000048.

[43] C. Corbo, R. Molinaro, A. Parodi, N.E. Toledano Furman, F. Salvatore, E. Tasciotti, The impact of nanoparticle protein corona on cytotoxicity, immunotoxicity and target drug delivery, Nanomedicine 11 (2016) 81–100, https://doi.org/10.2217/nnm.15.188.

[44] T. Kawasaki, Hydroxyapatite as a liquid chromatographic packing, J. Chromatogr. A 544 (1991) 147–184.

[45] C.D. Walkey, W.C.W. Chan, Understanding and controlling the interaction of nanomaterials with proteins in a physiological environment, Chem. Soc. Rev. 41 (2012) 2780–2799, https://doi.org/10.1039/c1cs15233e.

[46] A. Lesniak, A. Salvati, M.J. Santos-Martinez, M.W. Radomski, K.A. Dawson, C. Åberg, Nanoparticle adhesion to the cell membrane and its effect on nanoparticle uptake efficiency, J. Am. Chem. Soc. 135 (2013) 1438–1444, https://doi.org/10.1021/ja309812z.

[47] L. Chen, J.M. Mccrate, J.C.-M. Lee, H. Li, The role of surface charge on the uptake and biocompatibility of hydroxyapatite nanoparticles with osteoblast cells,

Nanotechnology 22 (2011), 105708, https://doi.org/10.1088/0957-4484/22/10/105708.

[48] S. Behzadi, V. Serpooshan, W. Tao, M.A. Hamaly, M.Y. Alkawareek, E.C. Dreaden, D. Brown, A.M. Alkilany, O.C. Farokhzad, M. Mahmoudi, Cellular uptake of nanoparticles: journey inside the cell, Chem. Soc. Rev. 46 (2017) 4218–4244, https://doi.org/10.1039/C6CS00636A.

[49] M. Safi, H. Sarrouj, O. Sandre, N. Mignet, J.-F. Berret, Interactions between sub-10-nm iron and cerium oxide nanoparticles and 3T3 fibroblasts: the role of the coating and aggregation state, Nanotechnology 21 (2010), 145103.

[50] T.T. Morgan, H.S. Muddana, E.İ. Altinoğlu, S.M. Rouse, A. Tabaković, T. Tabouillot, T.J. Russin, S.S. Shanmugavelandy, P.J. Butler, P.C. Eklund, J. K. Yun, M. Kester, J.H. Adair, Encapsulation of organic molecules in calcium phosphate nanocomposite particles for intracellular imaging and drug delivery, Nano Lett. 8 (2008) 4108–4115, https://doi.org/10.1021/nl8019888.

[51] M. Kopp, O. Rotan, C. Papadopoulos, N. Schulze, H. Meyer, M. Epple, Delivery of the autofluorescent protein rphycoerythrin by calcium phosphate nanoparticles into four different eukaryotic cell lines (HeLa, HEK293T, MG-63, MC3T3): highly efficient, but leading to endolysosomal proteolysis in HeLa and MC3T3 cells, PLoS One 12 (2017) 1–18, https://doi.org/10.1371/journal.pone.0178260.

[52] V. Sokolova, D. Kozlova, T. Knuschke, J. Buer, A.M. Westendorf, M. Epple, Mechanism of the uptake of cationic and anionic calcium phosphate nanoparticles by cells, Acta Biomater. 9 (2013) 7527–7535, https://doi.org/10.1016/j.actbio.2013.02.034.

[53] J. Guo, Y. Lao, D.C. Chang, Calcium and apoptosis, in: Handb. Neurochem. Mol. Neurobiol, Springer US, Boston, MA, 2009, pp. 597–622, https://doi.org/10.1007/978-0-387-30370-3_33.

[54] S. Patel, R. Docampo, Acidic calcium stores open for business: expanding the potential for intracellular Ca2+ signaling, Trends Cell Biol. 20 (2010) 277–286, https://doi.org/10.1016/j.tcb.2010.02.003.

[55] J. Yang, Z. Zhao, M. Gu, X. Feng, H. Xu, Release and uptake mechanisms of vesicular Ca2+ stores, Protein Cell 10 (2019) 8–19, https://doi.org/10.1007/s13238-018-0523-x.

[56] K.A. Christensen, J.T. Myers, J.A. Swanson, pH-dependent regulation of lysosomal calcium in macrophages, J. Cell Sci. 115 (2002) 599–607, https://doi.org/10.1073/pnas.89.21.10079.

[57] D. Thomas, S.C. Tovey, T.J. Collins, M.D. Bootman, M.J. Berridge, P. Lipp, A comparison of fluorescent Ca2+ indicator properties and their use in measuring elementary and global Ca2+ signals, Cell Calcium 28 (2000) 213–223, https://doi.org/10.1054/ceca.2000.0152.

[58] J. Groen, J.J. Conesa, R. Valcárcel, E. Pereiro, The cellular landscape by cryo soft X-ray tomography, Biophys. Rev. 11 (2019) 611–619, https://doi.org/10.1007/s12551-019-00567-6.

[59] J. Guo, C.A. Larabell, Soft X-ray tomography: virtual sculptures from cell cultures, Curr. Opin. Struct. Biol. 58 (2019) 324–332, https://doi.org/10.1016/j.sbi.2019.06.012.

[60] G. Schneider, P. Guttmann, S. Heim, S. Rehbein, F. Mueller, K. Nagashima, J. B. Heymann, W.G. Müller, J.G. McNally, Three-dimensional cellular ultrastructure resolved by X-ray microscopy, Nat. Methods 7 (2010) 985–987, https://doi.org/10.1038/nmeth.1533.

[61] M. Harkiolaki, M.C. Darrow, M.C. Spink, E. Kosior, K. Dent, E. Duke, Cryo-soft X-ray tomography: using soft X-rays to explore the ultrastructure of whole cells, Emerg. Top. Life Sci. 2 (2018) 81–92, https://doi.org/10.1042/etls20170086.

[62] J.C. Niclis, S.V. Murphy, D.Y. Parkinson, A. Zedan, A.H. Sathananthan, D.S. Cram, P. Heraud, Three-dimensional imaging of human stem cells using soft X-ray tomography, J. R. Soc. Interface 12 (2015) 1–11, https://doi.org/10.1098/rsif.2015.0252.

[63] B. Kepsutlu, V. Wycisk, K. Achazi, S. Kapishnikov, A.J. Pérez-Berná, P. Guttmann, A. Cossmer, E. Pereiro, H. Ewers, M. Ballauff, G. Schneider, J.G. McNally, Cells undergo major changes in the quantity of cytoplasmic organelles after uptake of gold nanoparticles with biologically relevant surface coatings, ACS Nano 14 (2020) 2248–2264, https://doi.org/10.1021/acsnano.9b09264.

[64] M. Chiappi, J.J. Conesa, E. Pereiro, C.O.S. Sorzano, M.J. Rodríguez, K. Henzler, G. Schneider, F.J. Chichón, J.L. Carrascosa, Cryo-soft X-ray tomography as a quantitative three-dimensional tool to model nanoparticle:cell interaction, J. Nanobiotechnol. 14 (2016) 15, https://doi.org/10.1186/s12951-016-0170-4.

[65] J. Gruenberg, The endocytic pathway: a mosaic of domains, Nat. Rev. Mol. Cell Biol. 2 (2001) 721–730, https://doi.org/10.1038/35096054.

[66] G. McDermott, M.A. Le Gros, C.G. Knoechel, M. Uchida, C.A. Larabell, Soft X-ray tomography and cryogenic light microscopy: the cool combination in cellular imaging, Trends Cell Biol. 19 (2009) 587–595, https://doi.org/10.1016/j.tcb.2009.08.005.